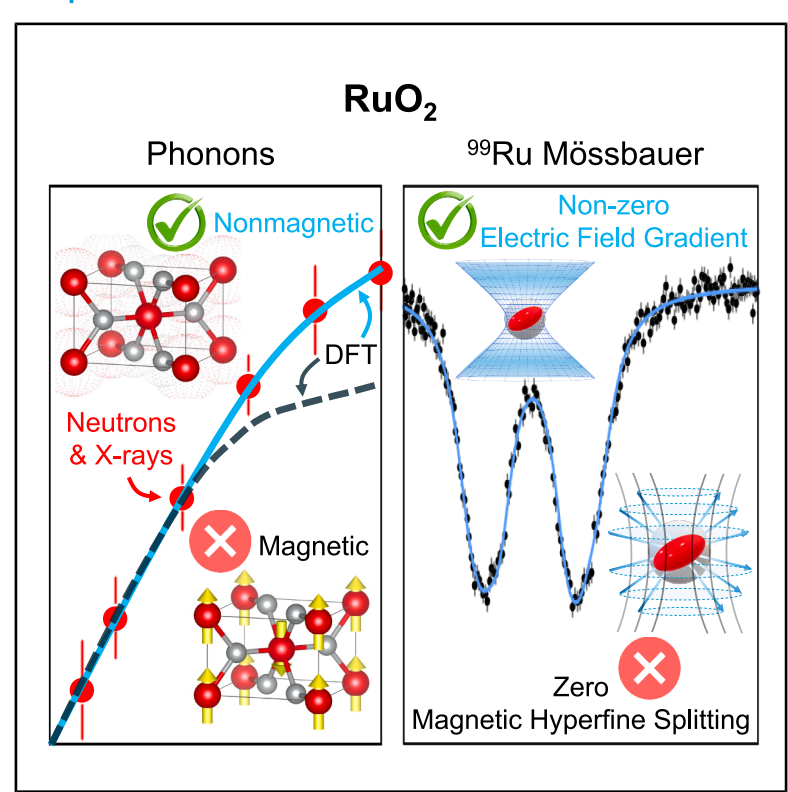
# Constraints on magnetism and correlations in RuO<sub>2</sub> from lattice dynamics and Mössbauer spectroscopy

#### **Graphical abstract**



#### **Authors**

George Yumnam, Parul R. Raghuvanshi, John D. Budai, ..., Valentino R. Cooper, Michael E. Manley, Raphaël P. Hermann

#### Correspondence

yumnamg@ornl.gov (G.Y.), hermannrp@ornl.gov (R.P.H.)

#### In brief

Yumnam et al. demonstrate that bulk RuO<sub>2</sub>, previously proposed as an altermagnet, is nonmagnetic based on neutron, X-ray, and Mössbauer spectroscopy combined with first-principles theory. Their results underscore the importance of carefully selecting exchange-correlation functionals in DFT studies of correlated materials.

#### **Highlights**

- Mössbauer and NFS rule out static or fluctuating Ru moments above  $\sim$ 0.03  $\mu_{\rm B}$
- Phonon measurements provide a stringent test of magnetic and electronic structure
- DFT functionals with magnetism fail to capture observed lattice dynamics
- Nonmagnetic r<sup>2</sup>SCAN alone reproduces the phonon data accurately



Please cite this article in press as: Yumnam et al., Constraints on magnetism and correlations in RuO<sub>2</sub> from lattice dynamics and Mössbauer spectroscopy, Cell Reports Physical Science (2025), https://doi.org/10.1016/j.xcrp.2025.102852

### Cell Reports Physical Science



#### Report

# Constraints on magnetism and correlations in RuO<sub>2</sub> from lattice dynamics and Mössbauer spectroscopy

George Yumnam,<sup>1,10,\*</sup> Parul R. Raghuvanshi,<sup>1</sup> John D. Budai,<sup>1</sup> Lars Bocklage,<sup>2,3</sup> Douglas Abernathy,<sup>4</sup> Yongqiang Cheng,<sup>4</sup> Ayman H. Said,<sup>5</sup> Igor I. Mazin,<sup>6,7</sup> Haidong Zhou,<sup>8</sup> Benjamin A. Frandsen,<sup>9</sup> David S. Parker,<sup>1</sup> Lucas R. Lindsay,<sup>1</sup> Valentino R. Cooper,<sup>1</sup> Michael E. Manley,<sup>1</sup> and Raphaël P. Hermann<sup>1,\*</sup>

#### **SUMMARY**

We provide experimental evidence for the absence of a magnetic moment in bulk RuO<sub>2</sub>, a candidate alter-magnetic material, by using a combination of Mössbauer spectroscopy, nuclear forward scattering, inelastic X-ray and neutron scattering, and density functional theory calculations. Using complementary Mössbauer and nuclear forward scattering, we determine the Ru magnetic hyperfine splitting to be negligible. Inelastic X-ray and neutron scattering-derived lattice dynamics of RuO<sub>2</sub> are compared to density functional theory calculations of varying flavors. Comparisons among theory with experiments indicate that electronic correlations, rather than magnetic order, are key in describing the lattice dynamics.

#### **INTRODUCTION**

The recent observations of broken Kramers degeneracy and spin-resolved anomalous Hall effect in antiferromagnets (AFMs) has challenged the conventional Néel theory. 1-4 These so-called "altermagnets" simultaneously exhibit broken time reversal ( $\mathcal{T}$ ) and inversion ( $\mathcal{P}$ ), resulting in non-relativistic spin splitting in their band structures. 1,5-7 This k-space-dependent spin splitting with zero net magnetization is of interest for spin-tronics due to its potential for terahertz spin-current generation and detection with negligible stray fields. 8-11

Ruthenium dioxide (RuO<sub>2</sub>) is one of the most extensively explored materials with respect to potential altermagnetic characteristics.  $^{12-17}$  However, the magnetic structure and size of the magnetic moment on Ru<sup>4+</sup> ions in bulk RuO<sub>2</sub> are debated,  $^{18-23}$  notably due to various reports on thin film properties.  $^{13,16,22}$  RuO<sub>2</sub> crystallizes in the prototypical rutile structure with the space group P4<sub>2</sub>/mnm (136), where each Ru atom is octahedrally coordinated by six oxygen atoms that form a distorted RuO<sub>6</sub> octahedron  $^{24,25}$  (see Figure 1A). The  $\mathcal P$  and  $\mathcal T$  symmetry breaking in RuO<sub>2</sub> arises from the two different orientations of the RuO<sub>6</sub> octahedra (see Figure 1B). In the presence of a spin on Ru, this unique configuration of alternating opposite spins

on Ru atoms, with different orientations of the RuO $_6$  octahedra, is central to the unconventional magnetic and transport properties in RuO $_2$ . Altermagnetism requires the magnetic structure of RuO $_2$  to have an anti-parallel coupling of Ru $_1$  and Ru $_2$  magnetic moments polarized along the c axis with a propagation wave vector  $q=(0,0,0)^7$ . Based on the recently proposed spin-space group,  $^{1,7}$  RuO $_2$  would have  $[C_2||C_{4z}t]$ , which corresponds to a spin-space 2-fold rotation symmetry  $(C_2)$  and a real-space 4-fold rotation symmetry along the c axis combined with a translation Ru $_1$   $\stackrel{t}{\rightarrow}$  Ru $_2$   $(C_{4z}t)$  as shown in Figure 1B.

Early single-crystal neutron diffraction measurements observed a small structurally forbidden (100) reflection, which indicates a magnetic reflection, hence suggesting the presence of a magnetic moment in RuO<sub>2</sub>. <sup>19</sup> This result could only be reproduced with density functional theory (DFT) calculations employing a Hubbard U correction (DFT + U) that induced an antiferromagnetic groundstate. <sup>19</sup> A magnetic moment of  $\sim 0.05 \mu_{\rm B}$  was estimated at room temperature with a magnetic structure corresponding to the P4<sub>2</sub>/mnm symmetry with oppositely coupled spins on Ru<sub>1</sub> and Ru<sub>2</sub> aligned along the c axis. Recent DFT + U based lattice dynamics calculations of RuO<sub>2</sub> with U = 2 eV, which gives a larger magnetic moment of 1.152  $\mu_{\rm B}/{\rm Ru}$ , showed reasonable agreement of the  $\Gamma$ -point Raman modes with

<sup>&</sup>lt;sup>1</sup>Materials Science and Technology Division, Oak Ridge National Laboratory, Oak Ridge, TN 37830, USA

<sup>&</sup>lt;sup>2</sup>Deutsches Elektronen-Synchrotron DESY, Notkestr. 85, Hamburg 22607, Germany

<sup>&</sup>lt;sup>3</sup>The Hamburg Centre for Ultrafast Imaging CUI, Hamburg 22761, Germany

<sup>&</sup>lt;sup>4</sup>Neutron Scattering Division, Oak Ridge National Laboratory, Oak Ridge, TN 37830, USA

<sup>&</sup>lt;sup>5</sup>Advanced Photon Source, Argonne National Laboratory, Lemont, IL 60439, USA

<sup>&</sup>lt;sup>6</sup>Department of Physics and Astronomy, George Mason University, Fairfax, VA 22030, USA

<sup>&</sup>lt;sup>7</sup>Quantum Science and Engineering Center, George Mason University, Fairfax, VA 22030, USA

<sup>&</sup>lt;sup>8</sup>Department of Physics and Astronomy, University of Tennessee, Knoxville, TN 37996, USA

<sup>&</sup>lt;sup>9</sup>Department of Physics and Astronomy, Brigham Young University, Provo, UT 84604, USA

<sup>10</sup>Lead contact

<sup>\*</sup>Correspondence: yumnamg@ornl.gov (G.Y.), hermannrp@ornl.gov (R.P.H.) https://doi.org/10.1016/j.xcrp.2025.102852



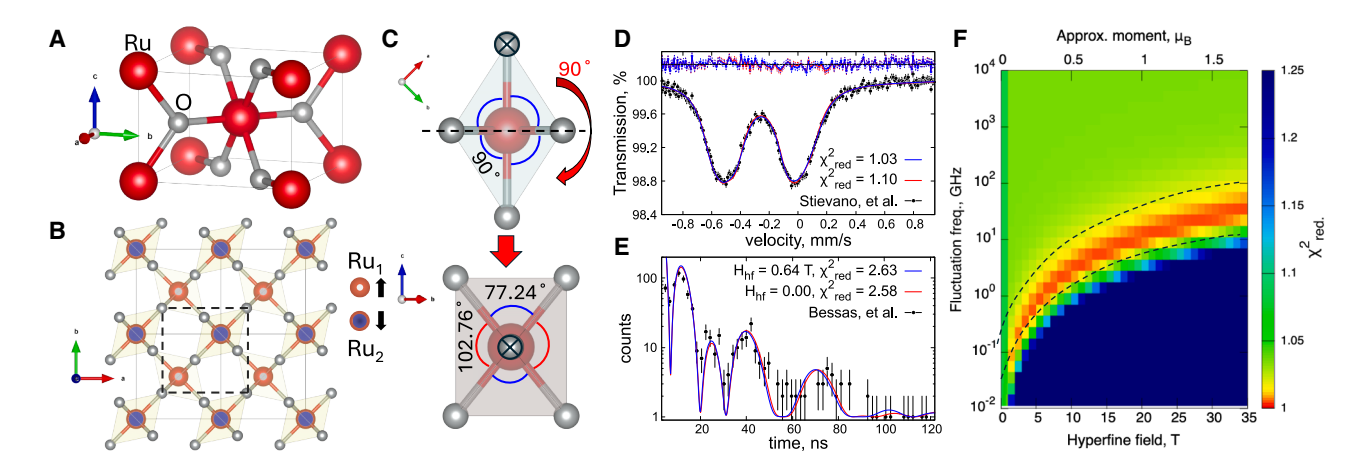


Figure 1. The crystal asymmetry and Mössbauer spectra of RuO<sub>2</sub>

(A) The rutile crystal structure of RuO<sub>2</sub> with Ru atoms in red, and O atoms in gray.

(B) The c axis projection illustrates the  $[C_2||C_{4z}t]$  symmetry, where Ru<sub>1</sub> (spin up) and Ru<sub>2</sub> (spin down) are associated with RuO<sub>6</sub> octahedra oriented differently. The dotted box highlights a unit cell with a shifted origin that clearly distinguishes Ru<sub>1</sub> and Ru<sub>2</sub> environments under  $[C_{4z}t]$  symmetry operation.

(C) Representation of the strong distortion in the  $RuO_6$  octahedra from two viewing angles. The octahedra consists of  $90^\circ$  O-Ru-O bonds along with 77.24° and  $102.76^\circ$  angle bonds in the plane of the octahedra. The O atom marked with  $\otimes$  shows the  $90^\circ$  transformation between the two viewing angles. Red, green, and blue arrows (crystallographic directions) represent a, b, and c directions.

(D and E) (D)  $^{99}$ Ru Mössbauer spectra of RuO<sub>2</sub> (data from Stievano et al.  $^{34}$ ) and (E) Nuclear forward scattering data of RuO<sub>2</sub> (data from Bessas et al.  $^{36}$ ) including the fits with (blue) and without (red) hyperfine field ( $H_{hf}$ ). Error bars represent the Poisson statistical error.

(F) Map of reduced  $\chi^2$  as a function of the spin relaxation frequency and hyperfine field ( $H_{hf}$ ). The red region ( $\chi^2_{red.} \simeq 1$ ) represents best fit (dashed lines are a guide to the eye).

experiment. <sup>26</sup> A modified magnetic structure model in RuO<sub>2</sub> was also proposed based on a monoclinic (P2<sub>1</sub>/c) unit cell, which permits a centrosymmetric magnetic structure that preserves translational symmetry and retains the propagation vector q=(0,0,0). <sup>23</sup> At the same time, non-polarized neutron diffraction could only be fit with a magnetic moment of  $\sim 0.23~\mu_{\rm B}^{-19}$ , and the lowest magnetic moment observed in the DFT + U calculations ( $U_{\rm eff}=1.2~{\rm eV}$ ) was  $\sim 0.7~\mu_{\rm B}$  with an antiferromagnetic configuration. <sup>19</sup> This quantitative discrepancy regarding the size of the presumed magnetic moment was not resolved.

Subsequent reassessments of bulk RuO2 using single-crystal neutron diffraction revealed that the previously observed intensity of the structurally forbidden (100) reflection 19 is likely a double-scattering artifact. 20,27 Furthermore, two independent experiments using muon spin rotation (µSR) spectroscopy found that the magnetic order in RuO2 is either absent entirely or the magnetic moments must be below  $10^{-3} \mu_B$ .  $^{20,21,27}$  However, there are several reports of unconventional magnetic and transport properties in two-dimensional RuO2, which could be due to the interfacial/epitaxial strain and its anisotropy. 13,16,28,29 A previous study on the structure and properties of monolayer RuO<sub>2</sub> nanosheets fabricated via chemical exfoliation demonstrated the possibility of structural transformation from octahedrally coordinated  $t - MX_2$  structure to a trigonal prismatically coordinated  $h - MX_2$  structure.<sup>30</sup> This structural reconstruction leads to a shift from metallic to semiconducting behavior, enabling tunable electrical and optical properties suitable for flexible, transparent electrode applications. 30 A more recent examination indicates that RuO2 exhibits a robust and anisotropic spin Hall effect even in the absence of altermagnetic spin splitting contributions.<sup>31</sup> Similarly, angle-resolved photoemission spectroscopy (ARPES) studies have demonstrated that depending on sample growth conditions, variations in the spin splitting can arise via strain or structural distortions.<sup>16,22</sup>

Here, we present experimental evidence for the absence of a magnetic moment in  ${\rm RuO_2}$  via a combination of inelastic neutron and X-ray scattering, Mössbauer spectroscopy, and nuclear forward scattering techniques. We also employed first-principles calculations of the lattice dynamics based on density functional theory. We used bulk  ${\rm RuO_2}$  single crystal and powders in our experiments to rule out the influence of strain and other distortions arising from low-dimensionality and substrate effects.

#### **RESULTS**

### Nuclear resonance spectroscopy: RuO<sub>2</sub> hosts zero magnetic moments

We utilized <sup>99</sup>Ru Mössbauer spectroscopy<sup>32</sup> to directly probe the magnetic hyperfine field ( $H_{\rm hf}$ ) at the nucleus. <sup>33</sup> This enables the detection of local magnetism, even in the absence of longrange order, both for itinerant and localized moments, and is sensitive to potential transferred hyperfine fields from neighboring atoms. Mössbauer spectroscopy also probes the atomic charge state, through the isomer shift ( $\delta_{\rm IS}$ ), and distortion of the local electronic environment through the quadrupole splitting ( $\Delta E_{\rm Q}$ ), which probes the electric field gradient (EFG). <sup>99</sup>Ru Mössbauer spectra of RuO<sub>2</sub> at  $\sim$  5 K were previously reported <sup>32,34</sup> and were analyzed with a single component fit with  $\delta_{\rm IS} = -0.26(1)$  mm/s and  $|\Delta E_{\rm Q}| = 0.50(1)$  mm/s, indicative of Ru(IV) in a distorted octahedral environment ( $\Delta E_{\rm Q} = 0$  for cubic local symmetry). The large distortion in the RuO<sub>6</sub> octahedra is associated with



the asymmetric bond angles between adjacent O-Ru-O bonds in the plane, where neighboring angles are 77.24° and 102.76°, respectively, as shown in Figure 1C. This distortion yields a fairly large EFG. The earlier fits of the Mössbauer data did not consider the sign of  $V_{77}$  and the asymmetry parameter of the EFG,  $\eta =$  $(|V_{vv}| - |V_{xx}|)/|V_{zz}|$ , where  $V_{...}$  represents principal components of the EFG tensor. The constraint  $|V_{zz}| > |V_{yy}| > |V_{xx}|$  mandates that  $0 \le \eta \le 1$ . For <sup>99</sup>Ru, the sign of  $V_{zz}$  and the magnitude of  $\eta$  can be determined, even in the absence of magnetic hyperfine splitting, because the nuclear transition occurs between the  $I_q$  = 5/2 ground state and  $I_e = 3/2$  excited nuclear state. The necessity of using a fairly large  $\eta$  is established by  $^{99}$ Ru nuclear magnetic resonance (NMR) measurements that found  $\eta \sim 0.74$ . Our calculation of the EFG with the r<sup>2</sup>SCAN meta-GGA (generalized gradient approximation) functional (r<sup>2</sup>SCAN) (see methods) in the non-magnetic state yields  $V_{zz} = -10.9 \cdot 10^{-21} \text{ V/m}^2$ , which corresponds to  $\Delta E_Q = 0.42$  mm/s, and  $\eta = 0.426$ ;  $V_{zz}$ is along the c axis in this calculation. EFG values for other functionals are provided in Table S1 in the supplemental information; the only notable discrepancy between models is that for DFT + U = 2 eV in the AFM state, the direction for  $V_{zz}$  is along (110), i.e., between the a and b axes. Note that there is a relative rotation of 90° in the ab plane for the Ru<sub>1</sub> and Ru<sub>2</sub> EFG, as prescribed by the structure (see Figure 1B).

We reanalyze the Mössbauer spectra of RuO<sub>2</sub> from Stievano et al.<sup>34</sup> (see Figure 1D) by considering  $\eta$  in compliance with the <sup>99</sup>Ru-NMR experiment to assess the presence of a possible hyperfine field ( $H_{hf}$ ), while also considering the sign of the EFG. The first conclusion is that indeed a negative  $V_{zz} = -0.54$  mm/s and  $\eta \sim 0.74$  clearly improve the fit to the data (see comparison of fits with different signs in Figure S1 of the supplemental information). We also used nuclear forward scattering (NFS) of synchrotron radiation, which corresponds to time-domain Mössbauer spectral data from Bessas et al.  $^{36}$ , measured on RuO $_2$  at 10 K. NFS has a better resolution for hyperfine interactions than Mössbauer spectroscopy but is insensitive to the sign of the EFG. We thus performed a combined fit of the Mössbauer spectra and NFS data with the Nexus platform<sup>37</sup> (see Figures 1D and 1E). We used two models: (1) model A, without  $H_{hf}$  (red), and (2) model B, with  $H_{hf}$  (blue). Both models employ an asymmetry parameter of  $\eta = 0.74$ . The model with  $H_{hf}$  is indistinguishable from the model without  $H_{\rm hf}$  within error bars, which implies that a hyperfine field is not needed. Model A finds a  $H_{hf} = 0.64(15)$  T. There is no strict proportionality between the hyperfine field and the magnetic moment, but an order of magnitude can be estimated by considering Mössbauer data on SrRuO<sub>3</sub>.<sup>38</sup> Ru is octahedrally coordinated by O in  $SrRuO_3$  and exhibits a hyperfine field of  $\sim 33\,$ T for a 1.6  $\mu_B$  moment. Accordingly, the best-fit value of 0.64 T in the present case would correspond to a moment of  $\lesssim 0.03 \mu_B$  for

Given the low moment magnitude, a further option should be considered, namely, whether fast fluctuations of a disordered local moment could explain the observed spectrum. To assess this, we employed the random phase approximation (RPA) formalism on the stochastic theory of relaxation<sup>39</sup> to fit the data for varying spin relaxation frequencies, as used in Hermann et al.,  $^{40}$  on our Mössbauer spectrum. The resulting goodness-of-fit is represented by the reduced  $\chi^2$  as a function of the fluctua-

tion frequency and hyperfine field, as shown in Figure 1F. The RPA stochastic-relaxation analysis reveals that the best fits define a region in hyperfine-field vs. fluctuation rate. This region indicates that the larger the potential hyperfine field on Ru, the larger the fluctuation frequency would have to be to exceed GHz frequencies for a 10 T hyperfine field or  $\sim\!0.5~\mu_{\rm B}$  moment. Summarizing, considering only Mössbauer spectroscopy data, a large moment of  $\sim 1~\mu_{\rm B}$  would imply GHz-range fluctuation rates, whereas a static moment would be at most  $0.03(1)~\mu_{\rm B}$ , with no improvement in the fits compared to no moment.

### Lattice dynamics: Comparison of experimental and DFT phonon energies

Probing lattice dynamics and phonon dispersions of magnetic materials can give meaningful insights into the presence of spins and magnetic order, as spin-lattice interactions can alter force constants. This effect is observable even in weakly magnetic systems, where small magnetic moments and magnetic order arise from spin relaxation or short-range magnetic correlations. 41,42

We performed inelastic X-ray scattering (IXS) and inelastic neutron scattering (INS) experiments to measure the phonon spectra of bulk RuO2. Subsequently, to assess the sensitivity of phonons to different magnetic configurations, density functional theory (DFT) calculations were used to compute RuO2 phonons in both magnetic and non-magnetic ground states. The transverse (TA) and longitudinal (LA) acoustic phonons along the  $\Gamma$ -R and  $\Gamma$ -Z directions were obtained from IXS on single crystal  $RuO_2$  around the (0,0,2) and (0, -3,1) Bragg peaks, as illustrated in Figure 2B. In parallel, DFT-computed phonon band structures were obtained using r<sup>2</sup>SCAN with the rVV10 nonlocal correlation functional<sup>43</sup> (hereafter r<sup>2</sup>SCAN) and PBE-GGA + U (hereafter PBE + U) functionals, respectively (Figures 2C and 2D). Because PBE + U was shown to be extremely sensitive to the value of U, 18,44 we expanded calculations to r<sup>2</sup>SCAN, which has been shown to yield reliable predictions of both energetic and structural properties across a range of bonding environments. 43 Calculation details and ground state energies are provided in the supplemental information. Using the force constants and dynamical matrices computed via DFT, we obtain the dynamic structure factor, S(Q, E), and the Bose-factor corrected dynamic susceptibility,  $\chi''(Q, E)$ , via the OCLIMAX code, 45 which enables a direct comparison with experimentally measured phonons. Using r<sup>2</sup>SCAN, either a non-magnetic (NM) or an antiferromagnetic (AFM) state with a magnetic moment of  $\sim$ 0.963  $\mu_{\rm B}$  per Ru atom was obtained depending on whether an initial magnetic moment ( $\mu^i$ ) was specified. Corresponding phonon dispersions are shown in Figure 2C. Using the PBE + U framework, the system exhibits an NM ground state with U = 0 eV, whereas U = 2 eV stabilizes an AFM state with a magnetic moment of  $\sim$ 1.179  $\mu_{B}$  on Ru atoms. Corresponding phonon dispersions are shown in Figure 2D. There is a striking dependence on the magnetic state and chosen functional for the dispersion of the LA mode in the  $\Gamma$ -Z direction, as noted earlier in Raghuvanshi et al. 44 The magnetic moments and lattice parameters predicted using various DFT functionals are presented in Table S2 of the supplemental information.

A direct comparison of the IXS phonons (red circles with error bars) with DFT-based dynamic susceptibilities,  $\chi''(Q, E)$ , which



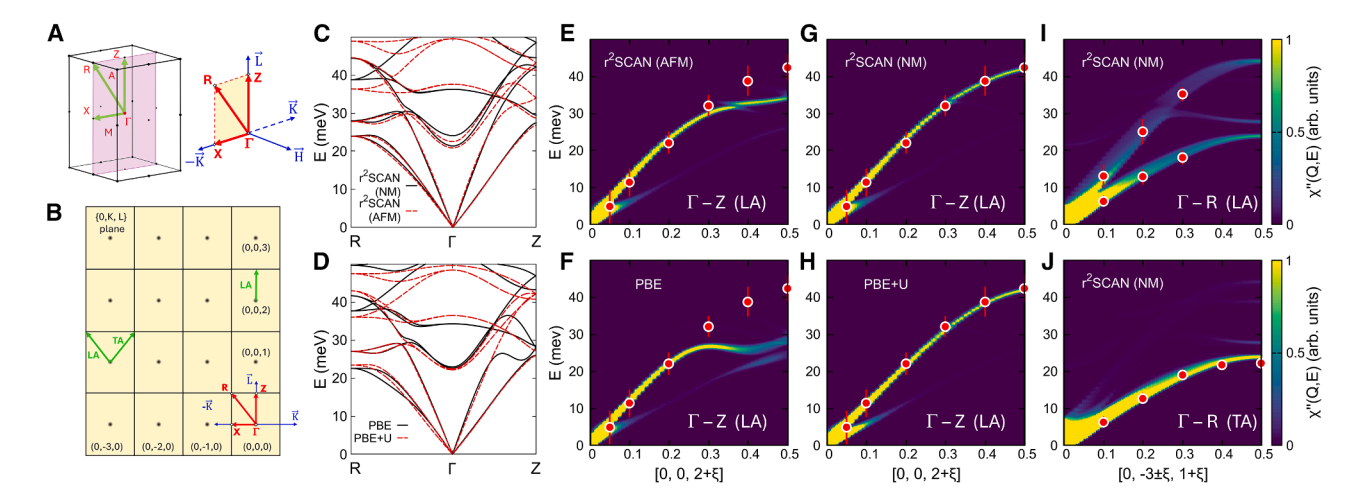


Figure 2. Dynamic structure factor, S(Q,E), of RuO<sub>2</sub>

(A) The Brillouin zone with high symmetry k points, drawn next to the (HKL) basis vectors of our IXS experiment.

(B) The reciprocal-space map of the (0KL) plane. Green arrows indicate the measured IXS path. Blue and red arrows are the projection of the basis vectors and high-symmetry k path in the plane.

(C and D) (C) r<sup>2</sup>SCAN and (D) PBE(+U) calculated phonon dispersions. Note the differences in the dispersion of acoustic phonons along Γ-Z.

(E–H) Overlay of the IXS phonons (red circles) on the IXS dynamic structure factor, S(Q,E), computed from  $r^2SCAN$  and PBE(+U) force constants along the  $\Gamma$ -Z direction for the LA mode reveals that  $r^2SCAN$  (NM) is the best model.

(I) LA-mode and (J) TA-mode phonons of  $r^2$ SCAN (NM) calculation along  $\Gamma$ -R direction (0,  $-3 \pm \xi$ ,  $1 + \xi$ ). The error bars shown in the plot are the full-width half-maxima (FWHM) of a DHO fit to the IXS constant-Q measurement. Errors of the data points are within the size of the circle. The unit of intensity as shown in the color bar is arbitrary (arb. units).

maps the populated phonons with corrections for the directional polarization, is shown in Figures 2E-2H. r<sup>2</sup>SCAN (AFM) and PBE (NM) phonons predict inaccurate dispersions (see Figures 2E and 2F), whereas  $r^2$ SCAN (NM) and PBE + U = 2 (AFM) both show very good agreement (see Figures 2G and 2H. The  $\Gamma$ -R phonons are properly described by all calculations, as depicted in Figures 2I and 2J, along with the r<sup>2</sup>SCAN (NM) dynamic susceptibility. Summarizing, IXS data for the  $\Gamma$ -Z LA phonon indicates that non-magnetic r<sup>2</sup>SCAN and the AFM state from PBE + U both reproduce the scattering intensities. A detailed discussion of the phonon behavior and symmetries along the  $\Gamma$ -Z and  $\Gamma$ -R directions based on the atom projected phonon band structure from each method is provided in the supplemental information (see Figures S3 and S4). We also performed Fermi surface calculations for each exchange-correlation functional, which reveal no conclusive evidence for Fermi-surface nestingmediated softening of the LA branch (see Figure S5 of the supplemental information).

Inelastic neutron scattering on  ${\rm RuO_2}$  powders yielded the dynamical susceptibility shown in Figure 3 (center). The measured  $\chi''$  can be classified into (1) low-energy phonons (0–50 meV), which display two features: low-lying conical dispersion attributed to the acoustic phonons and two flat optical modes with interconnected branches; and (2) high-energy phonons (50–90 meV), which display flat optical bands with few interconnects separated by a gap from the low-energy phonons. The calculated  $\chi''$  from our four models are shown for comparison; the  ${\rm r^2SCAN}$  (NM) calculated phonons provide an overall best visual match with the experiment.

However, a more direct comparison between the experimentally measured phonons and DFT calculations can be done

by comparing the integrated  $\chi''$ , i.e.,  $\int \chi''(Q,E)dQ$  from Q=7-12 Å as a function of energy transfer (*E*) as shown in Figure 4. For this comparison, exact matches in energy should be disregarded as the INS data were obtained at 295 K and are compared to ground-state DFT calculations, i.e., T=0 K. Considering the overall shape of the models, there is better agreement with r<sup>2</sup>SCAN (NM), whereas both PBE + U magnetic orderings fail at higher energies and r<sup>2</sup>SCAN (AFM) fails at all energies.

#### DISCUSSION

Here, we will discuss these observations in light of other recent research on RuO2 magnetism, notably µSR and neutron diffraction in Keßler et al. 20 and  $\mu$ SR in Hiraishi et al. 21 These studies provide strong evidence against and upper boundaries for a possible magnetic moment on Ru. A combination of 99Ru Mössbauer spectroscopy and NFS analyzed here likewise indicates that any static Ru moment would be very small, at most 0.03  $\mu_{\text{R}},$  whereas GHz-frequency fluctuations would be required for any larger moment. Overall, the data can be explained without any magnetic hyperfine splitting on the 99Ru nuclei. Concerning the possibility of any fluctuating moments, the  $\mu$ SR data, specifically with applied longitudinal field, also rule out any large uncorrelated moments-which would result in robust muon depolarization even in the presence of a weak applied longitudinal field, in contrast to the observed behavior reported in Hiraishi et al.21

A second observation concerns the LA phonons in the  $\Gamma$ -Z direction, which in our DFT calculations are highly sensitive to the combination of magnetism and exchange-correlation



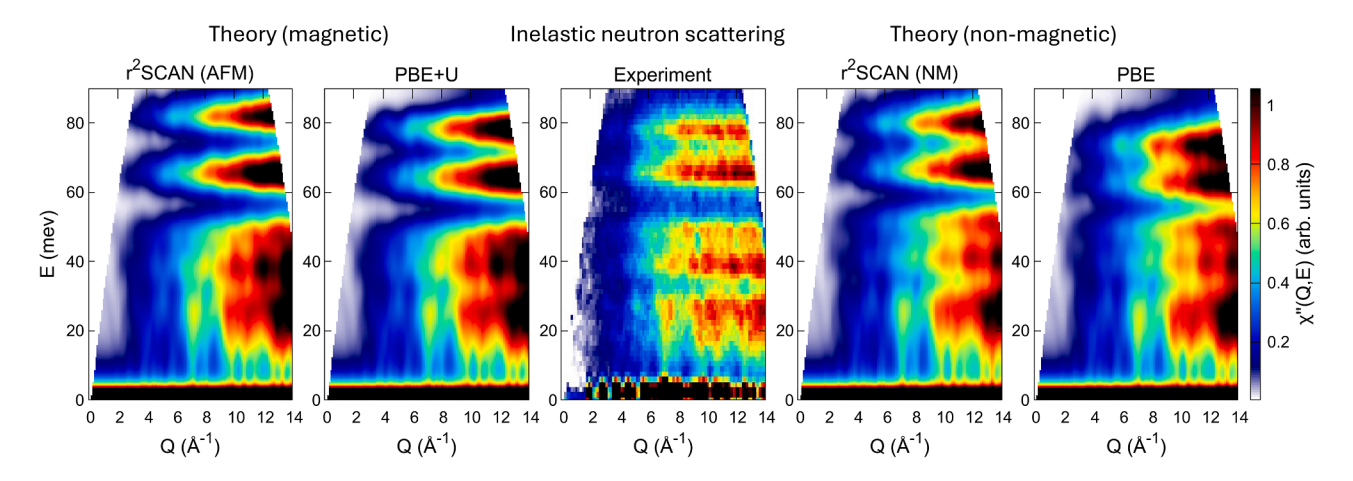


Figure 3. Experimental and calculated dynamic susceptibility

Dynamic susceptibility,  $\chi''(Q,E)$ , for RuO<sub>2</sub> powder spectra measured at ARCS ("experiment," in the middle) and the corresponding OCLIMAX calculated  $\chi''(Q,E)$  based on DFT force-constants for r<sup>2</sup>SCAN (AFM), PBE + U, r<sup>2</sup>SCAN (NM), and PBE. The intensity represents  $\chi''(Q,E)$  in arbitrary units. Calculated intensity is shown with the same scaling for all methods.

approximations used. We initially found that the lattice dynamics calculations in the AFM state for PBE + U provided a good agreement and that the PBE non-magnetic state fails (see Figures 2F and 2H), which provides support for a correlated AFM state. However, non-magnetic calculations with the meta-GGA  $r^2$ SCAN functional (see Figure 2G) reproduce the data equally well, and even better if considering the INS data. This indicates that correlations are important for determining the correct behavior of this phonon branch, while magnetism is not necessary. This is in agreement with a recent optical spectroscopy study that supports the absence of magnetism in  $RuO_2$  although classifying it as a weakly correlated metal.  $^{46}$ 

The DFT + U method relies on the Hubbard U on-site Coulomb repulsion that tends to localize Ru 4d electrons. Hence one can arrive at a transition from itinerant to localized electrons with increasing U. Static DFT + U treats correla-

tions by enhancing localization that tends to freeze local moments that may exist only transiently in real materials. This method was initially introduced in order to describe magnetism in strongly correlated systems, such as La<sub>2</sub>CuO<sub>4</sub>.<sup>47</sup> It proved to be indispensable for strongly correlated insulators, mostly based on 3d or f metals, but in some cases also 4d or even 5d metals. However, it was at some point realized that in itinerant metals the tendency is opposite; DFT nearly always over-estimates the magnetic moment, 48 because magnetic and nearly magnetic metals are strongly fluctuating systems<sup>49</sup> and DFT is a mean field theory. Therefore, in good metals DFT + U routinely worsens the agreement with the experiment with respect to their magnetic properties. The same behavior was found for the r<sup>2</sup>SCAN functional.<sup>50</sup> Thus, there is little physical justification for using magnetic versions of either PBE + U or  $r^2$ SCAN to describe RuO<sub>2</sub>.

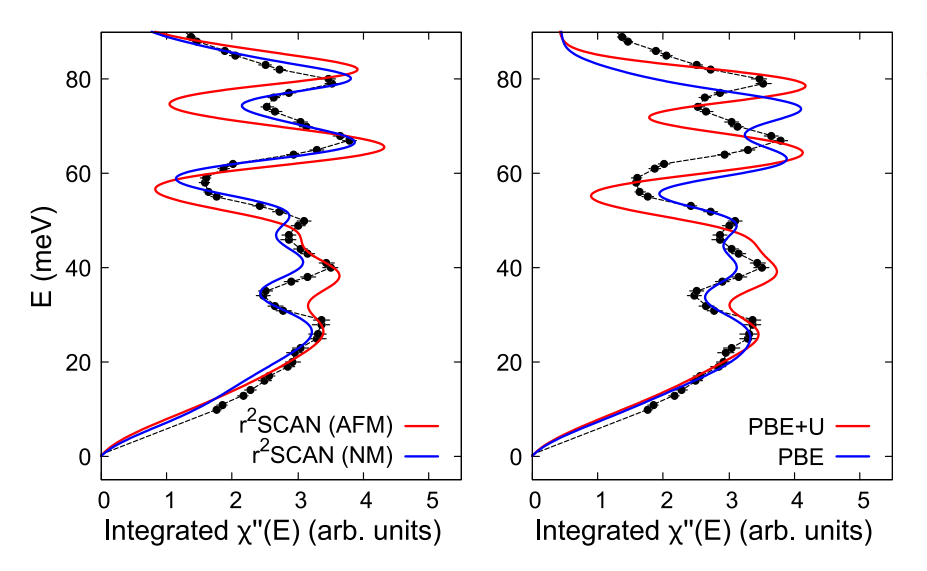


Figure 4. Best agreement of integrated  $\chi''(E)$  is given by r<sup>2</sup>SCAN (NM)

The integrated dynamic susceptibility  $\chi''(E)$  for  $\mathrm{RuO}_2$  from the ARCS measurement is represented by black circles. Correspondingly, the simulated integrated  $\chi''(E)$  for  $\mathrm{r}^2\mathrm{SCAN}$  (AFM),  $\mathrm{r}^2\mathrm{SCAN}$  (NM), PBE, and PBE+U is plotted. The simulated data are scaled by the same constant to compare with the experiment. Error bars represent the Poisson statistical error.





Therefore, it is not surprising that r<sup>2</sup>SCAN AFM calculations fail to describe the phonon data overemphasizing the electron-phonon coupling-induced Kohn anomaly near the Z point; that DFT without *U* has similar issues is probably a coincidence. A detailed comparison of the calculated electronic density of states from different functionals is provided in Figure S2 of the supplemental information. It remains unclear why non-magnetic r<sup>2</sup>SCAN appears superior in reproducing both phonon and EFG measurements; systematic studies of r<sup>2</sup>SCAN performance regarding these two calculations are lacking, and the community intuition is not well established yet.

In conclusion, we provide evidence that RuO2 is non-magnetic based on nuclear resonant experiments (99Ru Mössbauer spectroscopy and nuclear forward scattering techniques) coupled with inelastic X-ray and neutron scattering experiments and DFT calculations. Nuclear resonant experiments showed that RuO<sub>2</sub> has zero or, at best, a negligible hyperfine field. Inelastic X-ray scattering provides dispersions for the acoustic phonons along the  $\Gamma$ -Z and  $\Gamma$ -R directions, while inelastic neutron scattering provides powder averaged acoustic and optical phonons. In a direct comparison of the experimental phonon data with DFT calculated phonons using  $r^2SCAN$  and DFT+U functionals, we conclude that the lattice dynamics in RuO2 is best reproduced using r<sup>2</sup>SCAN with a zero magnetic moment on the Ru atoms, which accounts for some electronic correlations, specifically as needed for the  $\Gamma$ -L LA mode behavior. Our experimental results reveal that bulk RuO<sub>2</sub> is non-magnetic in nature and hence is not an altermagnet as previously thought. However, the precise nature of the electronic correlations remains unclear, and RuO<sub>2</sub> still appears to be a powerful and challenging test case for assessing calculation accuracy. Although RuO2 is intrinsically non-magnetic, the application of doping or strain could still induce a magnetic moment, rendering it a promising candidate for spintronic applications.

#### **Limitations of the study**

Mössbauer spectroscopy is slightly less sensitive in determining lower magnetic moment limits as compared to muon spin rotation/relaxation ( $\mu$ SR) measurements, although Mössbauer spectroscopy is a direct probe of the Ru nucleus and does not depend on muon stopping sites. The DFT calculations presented in this study were performed at T=0 K, whereas experimental phonon data are measured at 300 K.

#### **METHODS**

#### **Crystal growth**

Single crystals of  $RuO_2$  were grown using the chemical vapor transport method. Powders of  $RuO_2$  and Ru were mixed with a molar ratio of 1:9. The growth was carried out in a tube furnace with flowing oxygen as the transport agent. The tube furnace used was 2 feet long. The  $Al_2O_3$  tube used was 3 feet long. The starting materials were loaded in the  $Al_2O_3$  tube and located in the center of the tube furnace. The flowing oxygen was passing from right to left. The hot end was kept at 1,320°C, and the growth lasted 10 days. After the reaction, millimeter-sized samples with a range of morphologies, including bar and cuboidal shapes, were obtained at the cold

section of the tube, which is on the left side and  $\sim\!\!1$  foot from the center of the furnace.

### Mössbauer spectroscopy and nuclear forward scattering

The <sup>99</sup>Ru Mössbauer data in this work were obtained from Stievano et al.,<sup>34</sup> and the nuclear forward scattering data were obtained from Bessas et al.<sup>36</sup> We used the Nexus code<sup>37</sup> to perform the simultaneous fitting of the Mössbauer data and nuclear forward scattering data.

#### **Inelastic X-Ray scattering**

We performed the IXS measurements at beamline 30-ID(B)<sup>51</sup> of the advanced photon Source (APS) at Argonne National Laboratory. Single crystal RuO<sub>2</sub> was aligned in the (0, K, L) plane, which covers the  $\Gamma$ -Z and  $\Gamma$ -R directions as shown in Figure 2B. The experimental data were fitted using a damped harmonic oscillator (DHO) function convoluted with the instrument resolution. The IXS phonon data as shown in Figure 2E–2J are peak centers of the fits, and the error bars are the FWHM of the DHO profile. The error of the data point (peak center) is small and within the size of the circle.

#### **Inelastic neutron scattering**

We performed INS measurements on the wide-angle chopper spectrometer (ARCS) at the Spallation Neutron Source (SNS) of Oak Ridge National Laboratory. Powder  $RuO_2$  samples (5 g, 98% Colonial Metals) were loaded in an aluminum sample can and the inelastic spectra were measured at room temperature with an incident energy of 150 meV. An empty aluminum sample can was also measured with the same incident energy, and this was used to make a background subtraction. For extracting the integrated  $\chi''(E)$ , the Q integration range was chosen between 7 and 12  $\mathring{A}^{-1}$  to avoid the low intensities on the low-Q regions and to avoid the parabolic cutoff (high-Q and high-E region) due to the neutron kinetics.

#### **Density functional theory calculations**

We performed DFT calculations using the projector augmented wave (PAW) method<sup>52,53</sup> in VASP (v6.3.2)<sup>54,55</sup> with Ru (5s<sup>1</sup> 4d<sup>7</sup>) and O (2s<sup>2</sup> 2p<sup>4</sup>) potentials. All calculations used a plane-wave energy cutoff of 600 eV and an  $11 \times 11 \times 15$  Monkhorst-Pack k point mesh. Structural relaxations were performed until the forces on atoms were below 10<sup>-4</sup> eV/Å and the energy threshold reached 10<sup>-6</sup> eV. To assess the influence of exchange correlation, we compared calculations employing (1) PBE<sup>56</sup> with a Hubbard U correction ( $U_{eff} = 0$  and 2 eV) applied to the Ru d orbitals and (2) r<sup>2</sup>SCAN meta-GGA functional with the rVV10 nonlocal correlation functional, which has been shown to yield reliable predictions of both energetic and structural properties across a range of bonding environments. 43 r2SCAN functionals also better reproduce the equilibrium volume of RuO<sub>2</sub>. <sup>57</sup> The PBE + U calculation provides an important reference to demonstrate that electronic correlations govern the vibrational behavior in this system. Strengthening the correlations, whether with U = 2or switching to r<sup>2</sup>SCAN, improves agreement with measurements over plain PBE. We have not pursued other hybrid functionals, partly because Coulomb interactions are short range in



metallic systems and hybrid functionals include, as a part, a long-range Coulomb potential, which is unphysical in metals. Phonon band structures were obtained from second-order interatomic force constants (IFCs), calculated using the finite displacement method in Phonopy. For all phonon calculations,  $3 \times 3 \times 4$  supercells (216 atoms) with a  $2 \times 2 \times 2$  Monkhorst-Pack k point grids were employed.

The electric field gradients (EFGs) were computed using the  $WIEN2k^{59,60,61}$  software package, which outputs the principal components of the electric field gradient tensor, and thereby the associated asymmetry parameter  $\eta$ , at the central location of each of the atomic sites, with muffin-tin radii of 1.69 and 1.96 Bohr employed, respectively, for oxygen and ruthenium. As derivatives of a rapidly varying quantity (the electric field) these gradients are often quite sensitive to computational details and we have ensured convergence by employing an  $\mathbf{RK}_{\text{max}}$  (the value of the O sphere radius and largest plane-wave vector) of 9.0, as well as by checking convergence with respect to numbers of k points, with calculated gradient values changing by no more than a few percent when the number of full Brillouin zone k points was increased from 500 to 1,000. Similarly, the EFGs were also calculated using the VASP code and the projector-augmented-waves PAW basis, where the formalism introduced in Petrilli et al.  $^{62}$  is implemented. We used the  $\Gamma$  centered  $16 \times 16 \times 16 \, k$  mesh, well above the convergence criterion, hard pseudopotential for oxygen  $(O_b)$  and, for Ru, we included s and p semicore states (Rusy). The plane-wave cutoff was 700 eV.

The dynamic structure factor S(Q,E) calculated via the OCLIMAX code is based on the one-phonon coherent inelastic scattering limit as described in Cheng et al. <sup>45</sup> The dynamic structure factor for inelastic X-ray scattering one-phonon coherent inelastic scattering takes the same form as in the case of neutrons, where the structure factor in IXS is given by the atomic form factor,  $f_j(Q)$ , instead of the neutron scattering length density,  $b_j$ . The relation between  $\chi''(Q,E)$  and S(Q,E) is given by the fluctuation dissipation theorem. <sup>63</sup> Note that the OCLIMAX calculations of  $\chi''(E)$  from INS include contributions from multiphonon processes, i.e., the convolution of the one-phonon contribution with itself (and higher-order terms).

#### **RESOURCE AVAILABILITY**

#### Lead contact

Requests for further information and resources should be directed to and will be fulfilled by the lead author, George Yumnam (yumnamg@ornl.gov).

#### **Materials availability**

This study did not generate any new, unique material.

#### Data and code availability

- The data presented are available in the manuscript, the supplemental information, or the referenced sources.
- The data presented in this study are available at https://doi.org/10. 14461/oncat.data/2563163.
- No codes were generated in this study.

#### **ACKNOWLEDGMENTS**

We thank L. Stievano and D. Bessas for provision of datafiles of initial Mössbauer spectroscopy and NFS of  $RuO_2$ , respectively, and J. Hong for discussion on the phonon band structure in  $RuO_2$  DFT calculations. D. Mandrus, R. Val-

enti, I. Sergueev, J. Yan, D. Bansal, and P. Kent are acknowledged for helpful discussions. Research was supported by the US Department of Energy, Office of Science, Basic Energy Sciences, Materials Sciences and Engineering Division (BES-MSED). L.B. acknowledges funding from the cluster of excellence "CUI: Advanced Imaging of Matter" of the Deutsche Forschungsgemeinschaft (DFG)-EXC 2056-project ID 390715994 and support from DESY (Hamburg, Germany), a member of the Helmholtz Association HGF. I.I.M. was supported by Army Research Office under Cooperative Agreement number W911NF-22-2-0173. H.Z. (crystal growth) acknowledges the support from the US Department of Energy, BES-MSED with grant no. DE-SC0020254. B.A.F. ( $\mu$ SR and neutron analysis) was supported by the US Department of Energy, Office of Science, Basic Energy Science through award no. DE-SC0021134. Calculations used resources of the Compute and Data Environment for Science (CADES) at the Oak Ridge National Laboratory, which is supported by the Office of Science of the US Department of Energy under contract no. DE-AC05-000R22725 and the National Energy Research Scientific Computing Center (NERSC), a Department of Energy Office of Science User Facility using NERSC award BES-ERCAP-m1057. A portion of this research used resources at the Advanced Photon Source, a DOE Office of Science User Facility operated by Argonne National Laboratory. A portion of this research used resources at the Spallation Neutron Source, a DOE Office of Science User Facility operated by the Oak Ridge National Laboratory. The beam time was allocated to ARCS on proposal number IPTS-17267.1.

#### **AUTHOR CONTRIBUTIONS**

G.Y., investigation, formal analysis (Mössbauer, NFS, IXS, and INS), validation, visualization, writing – original draft, writing – review and editing; P.R.R., investigation, formal analysis (DFT), writing – review and editing; J.D.B., investigation (IXS and INS); L.B., formal analysis (NFS); D.A., investigation (INS); Y.C., formal analysis (INS); A.S., investigation (IXS); I.I.M., investigation, formal analysis (DFT), validation, writing – review and editing; H.Z., resources (crystal growth and synthesis); B.A.F., formal analysis ( $\mu$ SR and INS); D.S.P., investigation, formal analysis (DFT); L.R.L., formal analysis (DFT), validation, writing – review and editing; V.R.C., formal analysis (DFT), validation, writing – review and editing; R. P.H., conceptualization, validation, investigation, formal analysis, supervision, writing – review and editing.

#### **DECLARATION OF INTERESTS**

The authors declare no competing interests.

### DECLARATION OF GENERATIVE AI AND AI-ASSISTED TECHNOLOGIES IN THE WRITING PROCESS

During the preparation of this work, the author(s) used the Writefull editor in Overleaf that uses generative Al for text (grammar) and LaTeX formatting. After using this tool or service, the author(s) reviewed and edited the content as needed and take(s) full responsibility for the content of the publication.

#### SUPPLEMENTAL INFORMATION

Supplemental information can be found online at https://doi.org/10.1016/j.xcrp.2025.102852.

Received: May 22, 2025 Revised: July 17, 2025 Accepted: August 26, 2025

#### **REFERENCES**

 Šmejkal, L., Sinova, J., and Jungwirth, T. (2022). Emerging research landscape of altermagnetism. Phys. Rev. X 12, 040501. https://doi.org/10. 1103/PhysRevX.12.040501.



- Chen, H., Niu, Q., and MacDonald, A.H. (2014). Anomalous hall effect arising from noncollinear antiferromagnetism. Phys. Rev. Lett. 112, 017205. https://doi.org/10.1103/PhysRevLett.112.017205.
- Mazin, I.I., Koepernik, K., Johannes, M.D., González-Hernández, R., and Šmejkal, L. (2021). Prediction of unconventional magnetism in doped FeSb<sub>2</sub>. Proc. Natl. Acad. Sci. USA 118, e2108924118. https://doi.org/10. 1073/pnas.2108924118.
- Gonzalez Betancourt, R.D., Zubáč, J., Gonzalez-Hernandez, R., Geishendorf, K., Šobáň, Z., Springholz, G., Olejník, K., Šmejkal, L., Sinova, J., Jungwirth, T., et al. (2023). Spontaneous anomalous hall effect arising from an unconventional compensated magnetic phase in a semiconductor. Phys. Rev. Lett. 130, 036702. https://doi.org/10.1103/PhysRevLett.130.036702.
- Krempaský, J., Šmejkal, L., D'Souza, S.W., Hajlaoui, M., Springholz, G., Uhlířová, K., Alarab, F., Constantinou, P.C., Strocov, V., Usanov, D., et al. (2024). Altermagnetic lifting of kramers spin degeneracy. Nature 626, 517–522. https://doi.org/10.1038/s41586-023-06907-7.
- Osumi, T., Souma, S., Aoyama, T., Yamauchi, K., Honma, A., Nakayama, K., Takahashi, T., Ohgushi, K., and Sato, T. (2024). Observation of a giant band splitting in altermagnetic MnTe. Phys. Rev. B 109, 115102. https:// doi.org/10.1103/PhysRevB.109.115102.
- Šmejkal, L., Sinova, J., and Jungwirth, T. (2022). Beyond conventional ferromagnetism and antiferromagnetism: A phase with nonrelativistic spin and crystal rotation symmetry. Phys. Rev. X 12, 031042. https://doi. org/10.1103/PhysRevX.12.031042.
- Olejník, K., Seifert, T., Kašpar, Z., Novák, V., Wadley, P., Campion, R.P., Baumgartner, M., Gambardella, P., Němec, P., Wunderlich, J., et al. (2018). Terahertz electrical writing speed in an antiferromagnetic memory. Sci. Adv. 4, eaar3566. https://doi.org/10.1126/sciadv.aar3566.
- Jungwirth, T., Marti, X., Wadley, P., and Wunderlich, J. (2016). Antiferromagnetic spintronics. Nat. Nanotechnol. 11, 231–241. https://doi.org/10.1038/nnano.2016.18.
- Baltz, V., Manchon, A., Tsoi, M., Moriyama, T., Ono, T., and Tserkovnyak, Y. (2018). Antiferromagnetic spintronics. Rev. Mod. Phys. 90, 015005. https://doi.org/10.1103/RevModPhys.90.015005.
- Dal Din, A., Amin, O.J., Wadley, P., and Edmonds, K.W. (2024). Antiferromagnetic spintronics and beyond. npj Spintronics 2, 25. https://doi.org/10.1038/s44306-024-00029-0.
- Šmejkal, L., González-Hernández, R., Jungwirth, T., and Sinova, J. (2020). Crystal time-reversal symmetry breaking and spontaneous hall effect in collinear antiferromagnets. Sci. Adv. 6, eaaz8809. https://doi.org/10. 1126/sciadv.aaz8809.
- Feng, Z., Zhou, X., Šmejkal, L., Wu, L., Zhu, Z., Guo, H., González-Hernández, R., Wang, X., Yan, H., Qin, P., et al. (2022). An anomalous hall effect in altermagnetic ruthenium dioxide. Nat. Electron. 5, 735–743. https://doi.org/10.1038/s41928-022-00866-z.
- Šmejkal, L., Marmodoro, A., Ahn, K.H., González-Hernández, R., Turek, I., Mankovsky, S., Ebert, H., D'Souza, S.W., Šipr, O., Sinova, J., and Jungwirth, T. (2023). Chiral magnons in altermagnetic RuO<sub>2</sub>. Phys. Rev. Lett. 131, 256703. https://doi.org/10.1103/PhysRevLett.131.256703.
- Zhou, X., Feng, W., Zhang, R.W., Šmejkal, L., Sinova, J., Mokrousov, Y., and Yao, Y. (2024). Crystal thermal transport in altermagnetic RuO<sub>2</sub>. Phys. Rev. Lett. 132, 056701. https://doi.org/10.1103/PhysRevLett.132. 056701
- Fedchenko, O., Minár, J., Akashdeep, A., D'Souza, S.W., Vasilyev, D., Tkach, O., Odenbreit, L., Nguyen, Q., Kutnyakhov, D., Wind, N., et al. (2024). Observation of time-reversal symmetry breaking in the band structure of altermagnetic RuO<sub>2</sub>. Sci. Adv. 10, eadj4883. https://doi.org/10. 1126/sciadv.adj4883.
- Guo, Y., Zhang, J., Zhu, Z., Jiang, Y.y., Jiang, L., Wu, C., Dong, J., Xu, X., He, W., He, B., et al. (2024). Direct and inverse spin splitting effects in altermagnetic RuO<sub>2</sub>. Adv. Sci. 11, 2400967. https://doi.org/10.1002/advs. 202400967.

- Smolyanyuk, A., Mazin, I.I., Garcia-Gassull, L., and Valentí, R. (2024).
   Fragility of the magnetic order in the prototypical altermagnet RuO<sub>2</sub>.
   Phys. Rev. B 109, 134424. https://doi.org/10.1103/PhysRevB.109. 134424.
- Berlijn, T., Snijders, P.C., Delaire, O., Zhou, H.D., Maier, T.A., Cao, H.B., Chi, S.X., Matsuda, M., Wang, Y., Koehler, M.R., et al. (2017). Itinerant antiferromagnetism in RuO<sub>2</sub>. Phys. Rev. Lett. *118*, 077201. https://doi.org/10. 1103/PhysRevLett.118.077201.
- Keßler, P., Garcia-Gassull, L., Suter, A., Prokscha, T., Salman, Z., Khalyavin, D., Manuel, P., Orlandi, F., Mazin, I.I., Valentí, R., and Moser, S. (2024).
   Absence of magnetic order in RuO<sub>2</sub>: insights from μSR spectroscopy and neutron diffraction. NPJ Spintronics 2, 50. https://doi.org/10.1038/s44306-024-00055-y.
- Hiraishi, M., Okabe, H., Koda, A., Kadono, R., Muroi, T., Hirai, D., and Hiroi, Z. (2024). Nonmagnetic ground state in RuO<sub>2</sub> revealed by muon spin rotation. Phys. Rev. Lett. *132*, 166702. https://doi.org/10.1103/PhysRevLett. 132 166702
- Liu, J., Zhan, J., Li, T., Liu, J., Cheng, S., Shi, Y., Deng, L., Zhang, M., Li, C., Ding, J., et al. (2024). Absence of altermagnetic spin splitting character in rutile oxide RuO<sub>2</sub>. Phys. Rev. Lett. 133, 176401. https://doi.org/10.1103/ PhysRevLett.133.176401.
- Lovesey, S.W., Khalyavin, D.D., and van der Laan, G. (2023). Magnetic structure of RuO<sub>2</sub> in view of altermagnetism. Phys. Rev. B 108, L121103. https://doi.org/10.1103/PhysRevB.108.L121103.
- Bolzan, A.A., Fong, C., Kennedy, B.J., and Howard, C.J. (1997). Structural studies of rutile-type metal dioxides. Acta Crystallogr. B 53, 373–380. https://doi.org/10.1107/S0108768197001468.
- Jacob, K.T., Mishra, S., and Waseda, Y. (2000). Refinement of the thermodynamic properties of ruthenium dioxide and osmium dioxide.
   J. Am. Ceram. Soc. 83, 1745–1752. https://doi.org/10.1111/j.1151-2916. 2000.tb01459.x.
- Basak, S., and Ptok, A. (2024). Lattice dynamics of altermagnetic ruthenium oxide RuO<sub>2</sub>. Acta Phys. Pol. A 145, 93–96. https://doi.org/10.12693/APhysPolA.145.93.
- Kiefer, L., Wirth, F., Bertin, A., Becker, P., Bohatý, L., Schmalzl, K., Stunault, A., Rodríguez-Velamazan, J.A., Fabelo, O., and Braden, M. (2025).
   Crystal structure and absence of magnetic order in single-crystalline RuO<sub>2</sub>. J. Phys. Condens. Matter 37, 135801. https://doi.org/10.1088/1361-648X/adad2a.
- Gregory, B.Z., Strempfer, J., Weinstock, D., Ruf, J.P., Sun, Y., Nair, H., Schreiber, N.J., Schlom, D.G., Shen, K.M., and Singer, A. (2022). Straininduced orbital-energy shift in antiferromagnetic RuO<sub>2</sub> revealed by resonant elastic x-ray scattering. Phys. Rev. B 106, 195135. https://doi.org/ 10.1103/PhysRevB.106.195135.
- Chaudhary, P., Zagalskaya, A., Over, H., and Alexandrov, V. (2024). Strain-dependent activity-stability relations in RuO<sub>2</sub> and IrO<sub>2</sub> oxygen evolution catalysts. Chemelectrochem 11, e202300659. https://doi.org/10.1002/celc.202300659
- 30. Ko, D.S., Lee, W.J., Sul, S., Jung, C., Yun, D.J., Kim, H.G., Son, W.J., Chung, J.G., Jung, D.W., Kim, S.Y., et al. (2018). Understanding the structural, electrical, and optical properties of monolayer h-phase RuO<sub>2</sub> nanosheets: A combined experimental and computational study. NPG Asia Mater. 10, 266–276. https://doi.org/10.1038/s41427-018-0020-y.
- Wang, Y.C., Shen, Z.Y., Lin, C.H., Hsu, W.C., Chin, Y.Y., Singh, A.K., Lee, W.L., Huang, S.Y., and Qu, D. (2025). Robust anisotropic spin hall effect in rutile RuO<sub>2</sub>. Preprint at arXiv. https://doi.org/10.48550/arXiv.2503.07985.
- Kistner, O.C. (1966). Recoil-free absorption hyperfine spectra of the 90-kev mixed transition in Ru<sup>99</sup>. Phys. Rev. 144, 1022–1030. https://doi. org/10.1103/PhysRev.144.1022.
- Long, G.J., and Grandjean, F. (2013). Mössbauer Spectroscopy Applied to Magnetism and Materials Science, 1 (Springer Science & Business Media).
- Stievano, L., Calogero, S., Wagner, F.E., Galvagno, S., and Milone, C. (1999). Mössbauer characterization of carbon supported ruthenium-tin

Please cite this article in press as: Yumnam et al., Constraints on magnetism and correlations in RuO<sub>2</sub> from lattice dynamics and Mössbauer spectroscopy, Cell Reports Physical Science (2025), https://doi.org/10.1016/j.xcrp.2025.102852

### Cell Reports Physical Science Report



- catalysts. J. Phys. Chem. B *103*, 9545–9556. https://doi.org/10.1021/in990420e
- Mukuda, H., Ishida, K., Kitaoka, Y., Asayama, K., Kanno, R., and Takano, M. (1999). Spin fluctuations in the ruthenium oxides RuO<sub>2</sub> SrRuO<sub>3</sub>, CaRuO<sub>3</sub>, and Sr<sub>2</sub>RuO<sub>4</sub> probed by Ru NMR. Phys. Rev. B 60, 12279– 12285. https://doi.org/10.1103/PhysRevB.60.12279.
- Bessas, D., Merkel, D.G., Chumakov, A.I., Rüffer, R., Hermann, R.P., Sergueev, I., Mahmoud, A., Klobes, B., McGuire, M.A., Sougrati, M.T., and Stievano, L. (2014). Nuclear forward scattering of synchrotron radiation by <sup>99</sup>Ru. Phys. Rev. Lett. 113, 147601. https://doi.org/10.1103/PhysRevLett.113.147601.
- Bocklage, L. (2024). Nexus nuclear elastic x-ray scattering universal software (version: 1.2.0). Zenodo. doi: https://doi.org/10.5281/zenodo. 13832946 (last accessed: Jan, 2025).
- DeMarco, M., Cao, G., Crow, J.E., Coffey, D., Toorongian, S., Haka, M., and Fridmann, J. (2000). Temperature dependence of the hyperfine magnetic field in SrRuO<sub>3</sub> measured by the <sup>99</sup>Ru Mössbauer effect. Phys. Rev. B 62, 14297–14300. https://doi.org/10.1103/PhysRevB.62.14297.
- Dattagupta, S., and Blume, M. (1974). Stochastic theory of line shape. I. Nonsecular effects in the strong-collision model. Phys. Rev. B 10, 4540–4550. https://doi.org/10.1103/PhysRevB.10.4540.
- Hermann, R.P., Keppens, V., Bonville, P., Nolas, G.S., Grandjean, F., Long, G.J., Christen, H.M., Chakoumakos, B.C., Sales, B.C., and Mandrus, D. (2006). Direct experimental evidence for atomic tunneling of europium in crystalline Eu<sub>8</sub>Ga<sub>16</sub>Ge<sub>30</sub>. Phys. Rev. Lett. 97, 017401. https://doi. org/10.1103/PhysRevLett.97.017401.
- 41. Hahn, S.E., Lee, Y., Ni, N., Canfield, P.C., Goldman, A.I., McQueeney, R.J., Harmon, B.N., Alatas, A., Leu, B.M., Alp, E.E., et al. (2009). Influence of magnetism on phonons in CaFe<sub>2</sub>As<sub>2</sub> as seen via inelastic x-ray scattering. Phys. Rev. B 79, 220511. https://doi.org/10.1103/PhysRevB.79.220511.
- Yildirim, T. (2009). Frustrated magnetic interactions, giant magnetoelastic coupling, and magnetic phonons in iron-pnictides. Phys. C Supercond. 469, 425–441. https://doi.org/10.1016/j.physc.2009.03.038.
- Ning, J., Kothakonda, M., Furness, J.W., Kaplan, A.D., Ehlert, S., Brandenburg, J.G., Perdew, J.P., and Sun, J. (2022). Workhorse minimally empirical dispersion-corrected density functional with tests for weakly bound systems: r<sup>2</sup>SCAN+rVV10. Phys. Rev. B *106*, 075422. https://doi.org/10.1103/PhysRevB.106.075422.
- Raghuvanshi, P.R., Berlijn, T., Parker, D.S., Wang, S., Manley, M.E., Hermann, R.P., Lindsay, L., and Cooper, V.R. (2025). Altermagnetic behavior in OsO<sub>2</sub>: Parallels with RuO<sub>2</sub>. Phys. Rev. Mater. 9, 034407. https://doi.org/10.1103/PhysRevMaterials.9.034407.
- Cheng, Y.Q., Daemen, L.L., Kolesnikov, A.I., and Ramirez-Cuesta, A.J. (2019). Simulation of inelastic neutron scattering spectra using OCLIMAX. J. Chem. Theory Comput. 15, 1974-–1982. https://doi.org/10.1021/acs.jctc.8b01250.
- Wenzel, M., Uykur, E., Rößler, S., Schmidt, M., Janson, O., Tiwari, A., Dressel, M., and Tsirlin, A.A. (2025). Fermi-liquid behavior of nonaltermagnetic RuO<sub>2</sub>. Phys. Rev. B *111*, L041115. https://doi.org/10.1103/Phys-RevB.111.L041115.
- Anisimov, V.I., Zaanen, J., and Andersen, O.K. (1991). Band theory and Mott insulators: Hubbard U instead of Stoner I. Phys. Rev. B 44, 943–954. https://doi.org/10.1103/PhysRevB.44.943.

- Larson, P., Mazin, I.I., and Singh, D.J. (2004). Magnetism, critical fluctuations, and susceptibility renormalization in Pd. Phys. Rev. B 69, 064429. https://doi.org/10.1103/PhysRevB.69.064429.
- Moriya, T. (2012). Spin Fluctuations in Itinerant Electron Magnetism, 56 (Springer Science & Business Media).
- Fu, Y., and Singh, D.J. (2019). Density functional methods for the magnetism of transition metals: SCAN in relation to other functionals. Phys. Rev. B 100, 045126. https://doi.org/10.1103/PhysRevB.100.045126.
- Said, A.H., Sinn, H., Toellner, T.S., Alp, E.E., Gog, T., Leu, B.M., Bean, S., and Alatas, A. (2020). High-energy-resolution inelastic X-ray scattering spectrometer at beamline 30-ID of the Advanced Photon Source. J. Synchrotron Radiat. 27, 827–835. https://doi.org/10.1107/ S1600577520002854.
- Kresse, G., and Joubert, D. (1999). From ultrasoft pseudopotentials to the projector augmented-wave method. Phys. Rev. B 59, 1758–1775. https:// doi.org/10.1103/PhysRevB.59.1758.
- Blöchl, P.E. (1994). Projector augmented-wave method. Phys. Rev. B 50, 17953–17979. https://doi.org/10.1103/PhysRevB.50.17953.
- Kresse, G., and Furthmüller, J. (1996). Efficiency of ab-initio total energy calculations for metals and semiconductors using a plane-wave basis set. Comput. Mater. Sci. 6, 15–50. https://doi.org/10.1016/0927-0256 (96)00008-0.
- Kresse, G., and Furthmüller, J. (1996). Efficient iterative schemes for ab initio total-energy calculations using a plane-wave basis set. Phys. Rev. B 54, 11169-–11186. https://doi.org/10.1103/PhysRevB.54.11169.
- Perdew, J.P., Burke, K., and Ernzerhof, M. (1996). Generalized gradient approximation made simple. Phys. Rev. Lett. 77, 3865–3868. https://doi. org/10.1103/PhysRevLett.77.3865.
- Uykur, E., Janson, O., Ginga, V.A., Schmidt, M., Giordano, N., and Tsirlin,
   A.A. (2025). Tunable dirac nodal line in orthorhombic RuO<sub>2</sub>. Phys. Rev. B
   111, 134114. https://doi.org/10.1103/PhysRevB.111.134114.
- Togo, A. (2023). First-principles phonon calculations with phonopy and phono3py. J. Phys. Soc. Jpn. 92, 012001. https://doi.org/10.7566/JPSJ. 92.012001.
- Blaha, P., Schwarz, K., Sorantin, P., and Trickey, S.B. (1990). Full-potential, linearized augmented plane wave programs for crystalline systems. Comput. Phys. Commun. 59, 399–415. https://doi.org/10.1016/0010-4655(90)90187-6.
- Schwarz, K., and Blaha, P. (2003). Solid state calculations using wien2k.
   Comput. Mater. Sci. 28, 259–273. https://doi.org/10.1016/S0927-0256 (03)00112-5.
- Blaha, P., Schwarz, K., Tran, F., Laskowski, R., Madsen, G.K.H., and Marks, L.D. (2020). Wien2k: An apw+lo program for calculating the properties of solids. J. Chem. Phys. 152, 074101. https://doi.org/10.1063/1. 5143061.
- Petrilli, H.M., Blöchl, P.E., Blaha, P., and Schwarz, K. (1998). Electric-field-gradient calculations using the projector augmented wave method. Phys. Rev. B 57, 14690–14697. https://doi.org/10.1103/PhysRevB.57.14690.
- Kubo, R. (1966). The fluctuation-dissipation theorem. Rep. Prog. Phys. 29, 255–284. https://doi.org/10.1088/0034-4885/29/1/306.